Phase-Correlation Based Sea Ice Motion Tracking and Classification Using Spaceborne SAR Imagery

Anja Frost
Remote Sensing Technology Institute
German Aerospace Center (DLR)
Bremen, Germany
https://orcid.org/0000-0002-9748-1589

James Imber
Remote Sensing Technology Institute
German Aerospace Center (DLR)
Bremen, Germany
https://orcid.org/0000-0002-0803-5684

Dmitrii Murashkin
Remote Sensing Technology Institute
German Aerospace Center (DLR)
Bremen, Germany
https://orcid.org/0000-0002-5818-0038

Daniel Gregorek
MARUM, Center for Marine
Environmental Sciences
Bremen, Germany
https://orcid.org/0000-0003-1412-797X

Martin Bathmann
Remote Sensing Technology Institute
German Aerospace Center (DLR)
Bremen, Germany
https://orcid.org/0000-0002-7594-2444

***Abstract*—Sea ice is subject to continual change. It arises as seawater freezes, and is driven and deformed by winds, currents, ocean waves and temperature fluctuations. To observe the sea ice and its motion on a broad scale, Synthetic Aperture Radar (SAR) satellites are well suited, particularly as they provide images of land and frozen waters though clouds and regardless of solar illumination. In this paper, we present a software processor that is intended for the retrieval of high-resolution sea ice drift vector fields from pairs of subsequent, co-located SAR images. The core of the sea ice drift tracking algorithm is the well-known phase correlation technique executed hierarchically in a multiscale Gaussian pyramid. We explore the capabilities of the algorithm with a SAR image time series taken by the European satellite mission Sentinel-1 over the Arctic Ocean offshore close to Cape Morris Jesup during December 2021, when the ocean showed a closed cover of mainly multiyear ice. The retrieved sea ice drift vectors are validated with buoy data. In addition, we applied sea ice type classification on the SAR image series using the drift tracking algorithm for fusing classification results of the individual, subsequent SAR images. In so doing, we overcome inconsistent classification results and overall increase stability and reliability of the classification results.**

Keywords—earth observation, polar research, sea ice drift, convolutional neural network, machine learning, information fusion

I. INTRODUCTION

Ship navigation in polar waters is challenging. Drifted by wind and currents, the sea ice situation can change significantly within hours. When ice is driven together, previously navigable open water leads can rapidly close. With continued pressure in these convergence zones, sea ice floes are forced upward into a line called ridge, or piled haphazardly one over another, forming an uneven surface [1]. Such sea ice is hard to cross, even for icebreakers.

Synthetic Aperture Radar (SAR) satellites visualize different structures within the sea ice. Due to their active radar antenna, they provide image data of the oceans and frozen waters independent of cloud coverage, fog, or sun illumination. For decades, national ice services have utilized - amongst others - SAR data in order to generate ice maps, which are used for ship routing in polar waters. These ice maps are in general provided for large areas and yield a relatively coarse resolution. The manual generation of more detailed ice maps can only be offered to a limited extent by ice services (for example for search and rescue) and is very time-consuming. If the weather changes, ship routes can quickly be blocked by drifting ice. In other circumstances, safe and shorter routes that save fuel and time can open up, when forces are diverging.

In order to support ship routing during scientific polar expeditions, we established an operational data processing chain at DLR ground segment that allows to downlink and process SAR data of different missions and provide them to navigators on board in near real time (NRT). In special, we acquire SAR images of the German satellite mission TerraSAR-X along the ship course, as illustrated in Figure 1, or at target area [2][3]. The processing chain was used in multiple research expeditions, amongst others the one-year-long MOSAiC expedition of the Alfred Wegener Institute for Polar and Marine research, and it has been shown that the supply with “exclusive” up-to-date SAR images help to optimize ship routes and field measurements.

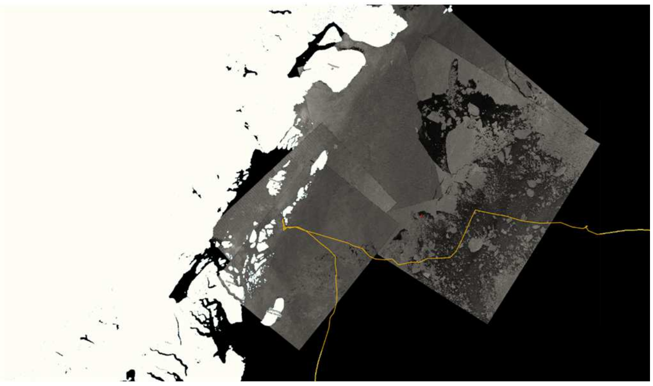

Figure 1: TerraSAR-X data takes during RV Polarstern expedition PS131 at the east coast of Greenland in summer 2022. Data takes were acquired along the ship course on a daily basis, and delivered on board in near real time using the operational data processing chain at DLR ground segment network site. The yellow line shows the ship track.

But SAR data inhere in information that is not visually apparent from a single image, in particular information about local sea ice drift variations.

In this paper, we explore the capabilities of a sea ice drift tracking algorithm that is intended to derive high resolution drift vector fields from pairs of subsequent, co-located SAR images of the missions TerraSAR-X, RADARSAT-2 and Sentinel-1. We showed performance of the algorithm combining TerraSAR-X ScanSAR and RADARSAT-2 ScanSAR Wide acquisitions in [3] and [4]. For our study here, we concentrate on Sentinel-1 data, taken over the Arctic Ocean offshore close to Cape Morris Jesup between the Lincoln and Wandel Seas during December 2021 when the ocean showed a closed cover of sea ice, which most probably consisted of mainly multiyear ice. East of Cape Morris Jesup, the concentration of multiyear ice may have decreased.

Sentinel-1 circles the Earth approx. 15 times per day at 700 km altitude. Due to its near-polar orbit, spatially and temporally close proximity acquisitions are possible in high latitudes, which allows frequent monitoring of the polar regions. On this basis, the sea ice drift can be determined with high accuracy by applying the well-known phase correlation technique [5]. Retrieved drift vector fields reveal convergence and divergence zones as well as sheering zones in a very fine scale. To quantize the accuracy of our drift retrieval, we use more than 1000 sea ice drift buoy measurements.

Extracted drift vectors allow to track e.g. an ice floe from one SAR image to the next and, in so doing, collect more information about the ice floe than just from one SAR acquisition, and analyse sea ice properties more detailed. This can be used for example to improve the sea ice type classification. In this paper, we show first test results on multitemporal sea ice classification outperformed on two subsequent SAR images. First, we apply sea ice classification individually on each SAR image of the time series. The software processor for sea ice classification utilizes a convolutional neural network (CNN) presented before [6] and - by exploiting the two polarizations of Sentinel-1 data - differentiates the following ice types: multiyear ice, first-year ice, new ice, open leads, and rough ice. Then, we combine classification results of two subsequent images by modelling probabilities for each ice type and each image (pixel by pixel), and fuse the probabilities considering the underlying drift vector field. In so doing, we try and overcome inconsistent classification results and further improve the classification.

II. SEA ICE MOTION TRACKING

A. State of the Art

There are different approaches for sea ice drift tracking using sequential SAR images. First of all, SAR interferometry might be considered. From along-track interferometry, it is known that a baseline/time interval of a few tens of meters/milliseconds allows to measure ocean currents, and a baseline/time interval of tens of kilometre/seconds allows to measure sea ice drift [7]. But for a reliable analysis of the interferometric phase, high coherence between image pairs is needed. In contrast, approaches on intensity are less sensitive and therefore allows to combine SAR images of different incidence angles, different orbits, different Bands, and different missions. In this paper, we propose an intensity driven pattern matching technique; more precisely phase correlation that relies on the frequency-domain representation of the SAR data.

Phase correlation has been first applied in [5] and is commonly used in diverse application areas of image processing, e.g. medical imaging or optical positioning. It is used for sea ice motion tracking from SAR data in [8-11]. We presented successful first tests on phase correlation combining TerraSAR-X ScanSAR and RADARSAT-2 ScanSAR Wide acquisitions in [4]. This paper focusses on the use of Sentinel-1 data acquired in Extra Wide (EW) swath mode. Here, we execute the phase correlation hierarchically within a Gaussian resolution pyramid. The following chapter explains the work flow in detail.

B. Functionallity of Phase Correlation Technique

Assume two squared images the size of *N*x*N* pixel that show the same object, e.g. the same piece of an ice floe, but shifted and rotated with an unknown displacement as illustrated in Figure 2.

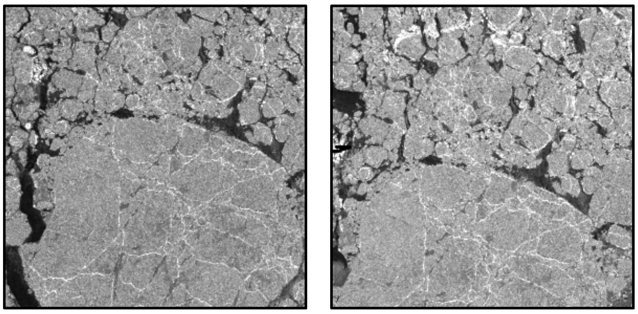

Figure 2: Cut-outs of two spaceborne SAR acquisitions taken approx. 24 hours apart showing drifting sea ice floes in the Arctic Ocean off Prince Patrick Island coast. Floes drifted mainly southwards (down) and slightly to the West (left). Small features on the floes allow to track them in a fine scale.

Translation, rotation and scaling have their counterparts in the frequency domain. That is, unknown translation, rotation and scaling parameters can be efficiently determined by applying a Fourier transform to the images. For pure tracking of floating sea ice from remote sensing data, just translation parameters are needed. Then, it is possible to apply phase correlation technique. Phase correlation relies on the shift theorem:

Let the two images g and h be shifted versions of each other, that is:

$$g(x, y) = h(x + u, y + v) \tag{1}$$

The Fourier transforms of g and h depend on each other. With $G(\omega_x, \omega_y)$ is the Fourier transform of $g(x, y)$ and $H(\omega_x, \omega_y)$ is the Fourier transform of $h(x, y)$, than the following equation holds:

$$H(\omega_x, \omega_y) = e^{-j(\omega_x u + \omega_y v)} G(\omega_x, \omega_y) \tag{2}$$

That is, the Fourier transforms of the two images g and h differ only by a change in the phase that is directly related to the translation (u, v). Introducing the normalized cross power spectrum $R(\omega_x, \omega_y)$, it is:

$$R(\omega_x, \omega_y) = \frac{G(\omega_x, \omega_y) H^*(\omega_x, \omega_y)}{|G(\omega_x, \omega_y) H^*(\omega_x, \omega_y)|} = e^{j(\omega_x u + \omega_y v)} \tag{3}$$

Thus, the inverse Fourier transform of R shows a distinct peak indicating the translation parameter (u, v):

$$(u, v) = \max_{x,y}\{\Im^{-1}(R(\omega_x, \omega_y))\} \qquad (4)$$

C. Implementation of Phase Correlation for Sea Ice Drift Retrieval

Figure 3 shows the basic workflow of our software processor. In the core (blue box in Figure 3), squared image patches the size of NxN pixel are cut out from each SAR acquisition. Patch $g(x, y)$ is extracted from the first image, and patch $h(x, y)$ from the second image. We introduce the following notation:

$$g(x, y) = \text{image1}(X0 + x,\ Y0 + y) \qquad (5)$$

$$h(x, y) = \text{image2}(X0 + x + u,\ Y0 + y + v) \qquad (6)$$

With $x = 0\ldots N\text{-}1$, $y=0\ldots N\text{-}1$ and $(X0, Y0)$ denoting the patch position in the grid of the second image (image2). (u, v) is the drift vector, which is initialized with (0, 0), because it is unknown. For performant implementation of the Fast Fourier Transform (FFT), N is a power of 2, by default 128.

The Hann function [12] is then applied to both patches in order to prevent discontinuities at the patch boundaries when performing the following complex FFT. From the Fourier-transformed images, the normalized cross power spectrum is computed and transformed back to spatial domain:

$$r(x, y) = \Im^{-1}\left(\frac{G(\omega_x,\omega_y)H^*(\omega_x,\omega_y)}{|G(\omega_x,\omega_y)H^*(\omega_x,\omega_y)|}\right) \qquad (7)$$

$r(x, y)$ shows a peak at (u', v') indicating the unknown drift of the sea ice visible in the patches. The drift vector is then updated with the new values $(u+u', v+v')$.

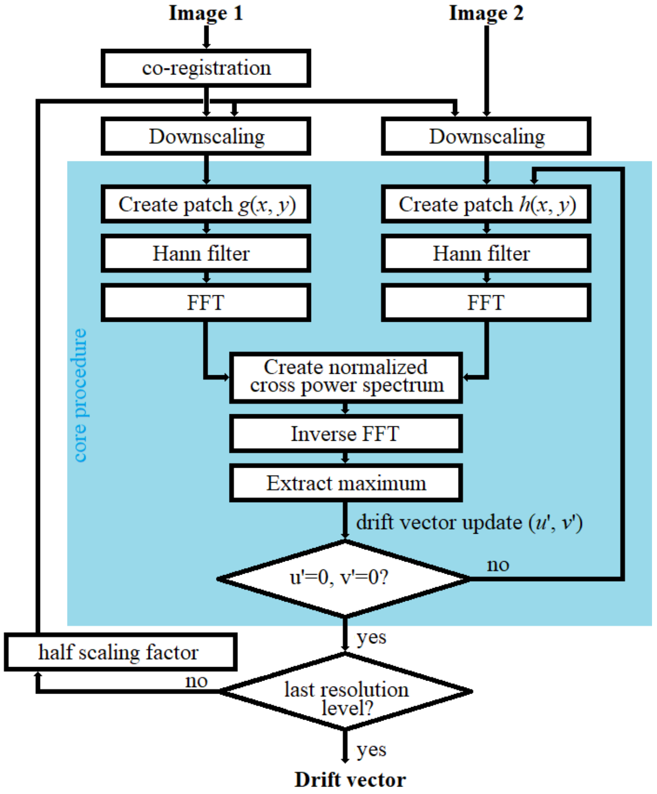

Figure 3: Flow chart of sea ice drift retrieval

The estimation is iteratively repeated with new patches h until a peak at $(u'=0, v'=0)$ indicates that the optimal pattern match is found.

To cover the entire image footprint, the patch position $(X0, Y0)$ is changed according to the desired resolution of the drift field and the above procedure is repeated for each location. In the experimental results presented here, we use a drift vector field resolution of 500 m.

D. Hierarchical Procesing

For the hierarchical processing, the drift field calculation is repeated for each layer of a multi-resolution Gaussian image pyramid with a reduction factor of 2 (see [13]). The size of the patches is kept constant at NxN pixels, so the coverage is high at the coarsest resolution and is halved with each higher resolution layer.

This hierarchical approach makes a compromise between using large-scale image patches which may contain sea ice drifts in multiple directions resulting in ambiguous drift vector estimation, and small-scale image patches which cannot cover large motions of the sea ice.

III. EXPERIMENTAL RESULTS

We apply our software processor for sea ice motion tracking as described in the previous chapter to a Sentinel-1 times series taken over the Arctic Ocean offshore close to Cape Morris Jesup between the Lincoln and Wandel Seas in early December 2021, when the ocean showed a closed cover of sea ice with some small leads of open water. The sea ice most likely consisted mainly of multiyear ice, particularly over the Lincoln Sea, while over the Wandel Sea it can be assumed that multiyear ice has been partially replaced by younger ice [14-15]. In Figure 4, the multiyear ice concentration from https://www.meereisportal.de (Förderung: REKLIM-2013-04) is given. This sea ice condition is well suited for drift tracking using pattern matching techniques.

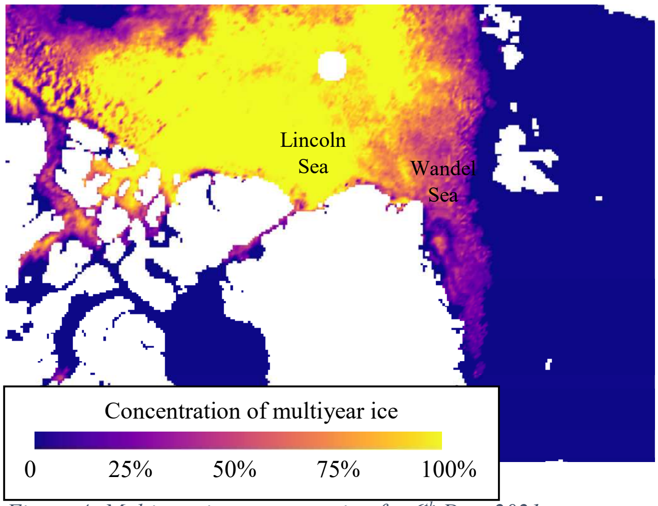

Figure 4: Multiyear ice concentration for 6th Dec. 2021

Table I lists the acquisitions used for our preliminary tests. Overall, 34 Sentinel-1 EM images are collected between 6th and 12th December 2021. A drift vector field is generated out of each image pair combination, i.e. $k = 34$ Sentinel-1 acquisitions result in

$$\binom{k}{2} = \left(\frac{k!}{2!(k-2)!}\right) \qquad (8)$$

= 561 drift vector fields.

TABLE I. SENTINEL-1 DATA ACQUISITIONS USED FOR SEA ICE MOTION TRACKING

Data set No.	***Acquisition date***	***Acquisition time***	***Heading angle***	***Orbit***
1	2021/12/06	11:25 UTC	244.969°	Ascending
2	2021/12/06	13:03 UTC	255.491°	Descending
3	2021/12/06	14:42 UTC	267.791°	Ascending
4	2021/12/06	16:19 UTC	288.617°	Ascending
5	2021/12/06	17:58 UTC	294.006°	Ascending
6	2021/12/07	10:28 UTC	240.774°	Ascending
7	2021/12/07	12:06 UTC	248.935°	Ascending
8	2021/12/07	13:44 UTC	257.545°	Ascending
9	2021/12/07	15:22 UTC	280.044°	Ascending
10	2021/12/07	17:01 UTC	292.722°	Ascending
11	2021/12/08	11:09 UTC	244.456°	Ascending
12	2021/12/08	12:47 UTC	252.560°	Descending
13	2021/12/08	14:25 UTC	264.624°	Ascending
14	2021/12/08	16:03 UTC	285.721°	Ascending
15	2021/12/08	17:41 UTC	296.584°	Ascending
16	2021/12/09	11:50 UTC	247.305°	Ascending
17	2021/12/09	13:28 UTC	259.378°	Ascending
18	2021/12/09	15:06 UTC	278.187°	Ascending
19	2021/12/09	16:44 UTC	292.183°	Ascending
20	2021/12/09	18:22 UTC	298.354°	Ascending
21	2021/12/10	12:31 UTC	250.373°	Ascending
22	2021/12/10	14:09 UTC	261.587°	Ascending
23	2021/12/10	15:47 UTC	284.037°	Ascending
24	2021/12/10	17:25 UTC	295.132°	Ascending
25	2021/12/11	09:55 UTC	231.046°	Ascending
26	2021/12/11	13:11 UTC	256.435°	Descending
27	2021/12/11	14:49 UTC	275.148°	Ascending
28	2021/12/11	16:28 UTC	289.507°	Ascending
29	2021/12/11	18:06 UTC	294.829°	Ascending
30	2021/12/12	10:36 UTC	241.536°	Ascending
31	2021/12/12	12:14 UTC	249.814°	Ascending
32	2021/12/12	13:52 UTC	264.726°	Ascending
33	2021/12/12	15:30 UTC	281.013°	Ascending
34	2021/12/12	17:09 UTC	293.562°	Ascending

Two drift buoys [16] deployed during MELTEX 2021 campaign of the Alfred Wegener Institute were located in our study area, which we use for quantifying the accuracy of our drift tracking algorithm. In a large scale, more precisely from 6th to 12th December 2021 the sea ice drifted eastwards and almost parallel to the coast. However, in smaller time periods, particularly on 8th and 9th December 2021, the buoys also show opposite drift directions.

A. Observation of the Drift Vector Fields

Exemplarily, Figure 5 shows in greyscales the Seninel-1 HH channel of data set 10 calibrated to sigma naught, and overlaid in colours the drift vector field generated with our tracking algorithm from data set 1 and 10. Colour coded is the sea ice drift velocity. Overlaid arrows indicate the drift direction with 10 km spacing. Obviously, the sea ice drifted homogeneously eastwards with a drift velocity ranging from 120 m/h (in the western part) to 500 m/h (in the eastern part). This creates divergence zones, which are noticeable in the colour jumps in the drift velocity map. In addition, the sea ice drift velocity decreased near the coast.

In our approach for sea ice drift tracking, each vector is estimated independently from neighbouring drift vectors. The homogeneous drift vector fields, as shown in Figure 5, indicate that the approach works very stable. We analysed all 561 drift vector fields for our study (not plotted here). The following analysis with buoy data provides further information on stability and accuracy.

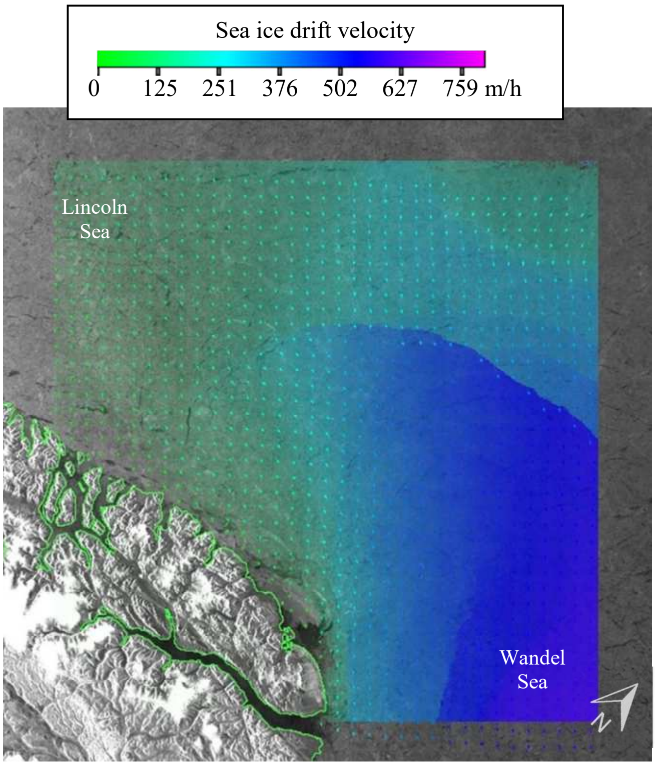

Figure 5: Sea ice drift vector field retrieved from Sentinel-1 data taken over the Arctic Ocean between the Lincoln and Wandel Sea on 6th Dec. 2021 11:25 UTC (data set 1) and 7th Dec. 2021 17:01 UTC (data set 10). Grey scales show Sentinel data from 7th Dec. 2021 17:01 UTC (data set 10). Overlaid colours represent retrieved drift velocity in 500 m resolution and arrows illustrate drift vectors (10 km spacing). Convergence and divergence zones become visible at the colour jumps in the drift velocity map.

B. Buoy Validation

The two sea ice drift buoys located in our study area report their position on an hourly basis via GPS, though the data contains a few gaps of up to four hours with no retrieved GPS signal. From all the provided buoy data, we approximate the buoy locations for the given SAR acquisition time using linear interpolation, and start drift vector estimation from that approximated position. We compare the resulting drift vector ending points with the approximated buoy position at the later SAR acquisition time, and calculate the absolute error Δs (see Figure 6).

We use all 561 SAR image pair combinations, but only results where the full patch size fit into the SAR footprint.

Figure 7 plots the measured absolute error Δs as a function of the real sea ice displacement. The larger the sea ice displacement, the more the accuracy of the retrieved drift vectors decreases. This is because with larger sea ice displacements, more deformation occurs and "patterns", i.e. significant structures in the ice that can be tracked, are more likely to be lost. Nevertheless, in 32 % of all our measurements, the absolute error is below 100 m, in 53 % below 200 m.

Up to a sea ice displacement of 10 km, an absolute error below 100 m is kept by 53% of our measurements, and an absolute error below 200 m by 87 % of the measurements. The one sigma error amounts to 132 m.

We note that high absolute errors were recorded for buoys close to shore, i.e. where sea ice may have shown ambiguous movement, as well as for large time difference between two SAR acquisitions, e.g. between data set 1 and 34.

In ongoing work, we expand the validation by using SAR image time series of other seasons and locations, as well as investigate different influencing parameters in order to further improve the sea ice drift retrieval algorithm.

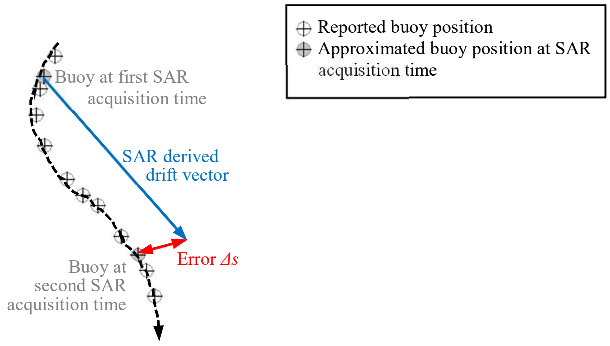

Figure 6: Definition of the absolute error Δs

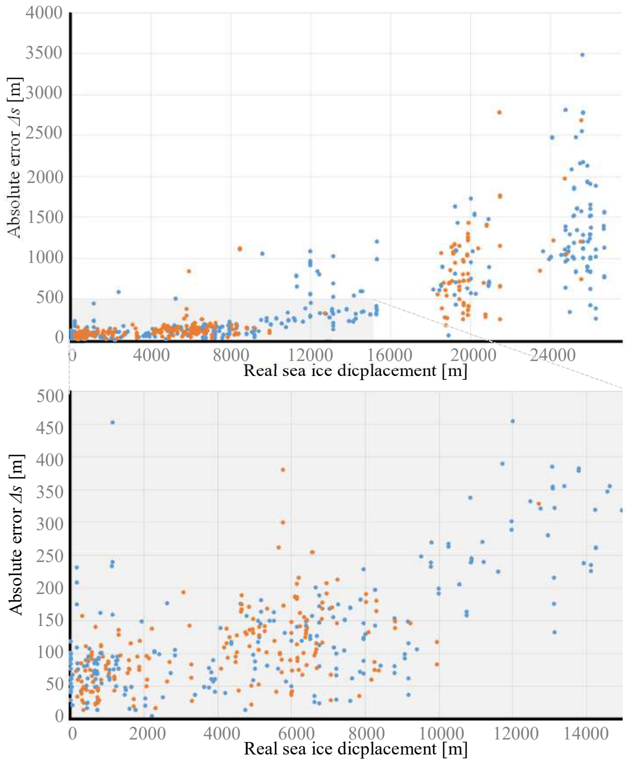

Figure 7: Absolute error versus real sea ice displacement in different scales. Blue: Measurements with SAR acquisition time at hourly reporting buoys. Orange: Measurements with SAR acquisition time at buoys reporting once in two, three, and five hours.

IV. APPLICATION FOR MULTI-TEMPORAL SEA ICE CLASSIFICATION

A high-resolution sea ice drift vector field generated from two subsequent SAR acquisitions is the key to analyse drifting sea ice and its properties in more detail. For example, one drifting ice object such as an ice floe can be tracked from one image to the next, and remote sensing data can then be collected over the floe, which results in more measurements. In our study, we aim at using the collected SAR information for a multitemporal sea ice classification.

Sea ice classification, performed on single Sentinel-1 acquisitions, was presented before in [6]. The core of the classification is an adjusted UNET++ convolutional neural network architecture described by [17]. In detail, the classification is done tile-wise, i.e. a Sentinel-1 acquisition is divided into tiles, classified, and then the results are joined back to generate an ice map. We differentiate six sea ice types: multiyear ice (MYI), first-year ice (FYI), young ice (YI), open leads (split in so-called dark leads (DL) and bright leads (BL)) and rough ice (RI).

A. *Comparing Classification Results*

Figure 8 shows the ice maps generated from the Sentinel-1 acquisitions taken on 6th Dec. 2021 11:25 UTC (data set 1) and 7th Dec. 2021 17:01 UTC (data set 10). In all data takes from Table I, MYI was predominantly detected over Lincoln Sea (i.e. on the western part of the study area), which coincides with the assumed sea ice situation (compare Figure 4). Over Wandel Sea, however, YI occurs inconsistently in different concentrations. E.g. on 6th Dec. 2021 11:25 UTC, the ice map shows mainly YI over Wandel Sea, while on the following day, 7th Dec 2021 17:01 UTC, the same ice was classified as MYI.

In order to detect and ideally correct inconsistent classification results such as the class change from YI to MYI, here we first combine the classification results of two SAR acquisitions. In detail, we compare the classification of the older SAR image at each drift vector start point with the classification of the newer SAR image at the associated drift vector end point. In case of unequal classification results, the ice class with higher SoftMax output is currently selected for the combined classification, i.e. we interpret the SoftMax output of the CNN as a probabilistic measure. The applicability in this form is discussed in the next subchapter B. “Modelling Probabilities”.

Figure 9 shows the combined sea ice classification from the data takes 1 and 10. The class change from YI to MYI as seen from 6th to 7th Dec 2021 becomes automatically corrected in most parts, even though a priori knowledge is not included yet, i.e. data driven only. The combined classification better represents the assumed real sea ice situation.

B. *Modelling Probabilities*

Over all, we noted increased stability in classification results by combining two SAR acquisitions. Nevertheless, in order to interpret the output values of the CNN as probabilistic measure, it must be confirmed that they do indeed behave as such. It has long been known that neural networks (particularly deep networks) can deviate significantly from this assumption [18]. An adjusted calibration can solve this problem. There are a number of methods in the literature that try and calibrate the probabilities in a reasonable way. In this paper, we outperform simple histogram scaling and temperature scaling on a labelled test data set generated from Sentinel-1 acquisitions taken in January 2020.

a) *Simple histogram scaling:* The plots in Figure 10 show the probability of being correct (y, left axis) as a function of the quoted output probability (x, in bins of 0.05) in orange vs the ideal case in blue for each of the class types. The blue bars are the number of pixels in each bin (y, right

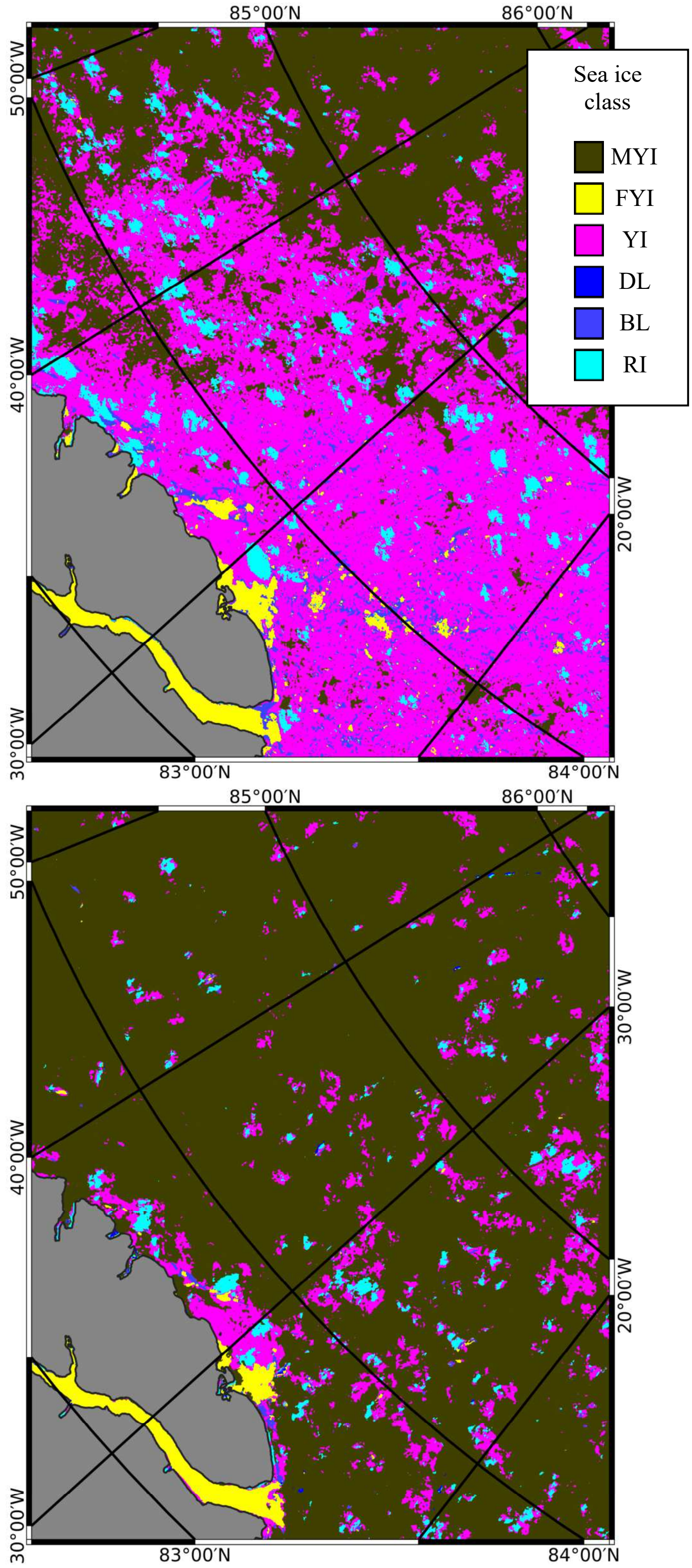

Figure 8: Sea ice classification performed on single Sentinel-1 acquisitions taken on 6th Dec. 2021 11:25 UTC (top) and 7th Dec. 2021 17:01 UTC (bottom).

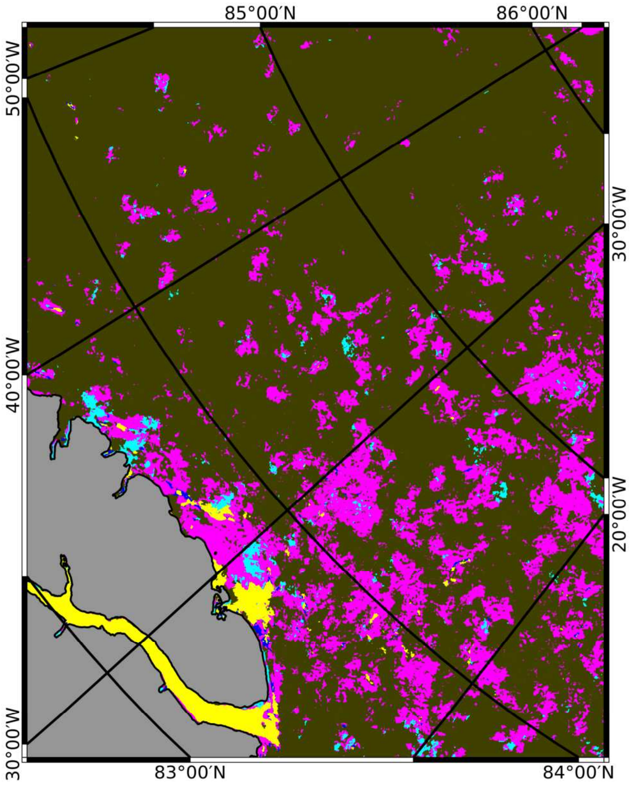

Figure 9: Combined sea ice classification from two Sentinel-1 acquisitions taken on 6th Dec. 2021 11:25 UTC and 7th Dec. 2021 17:01 UTC incorporating sea ice drift vector field from Figure 5. The unlikely high percentage of "young ice" over Lincoln Sea on 6th Dec.2021 gets corrected in most parts.

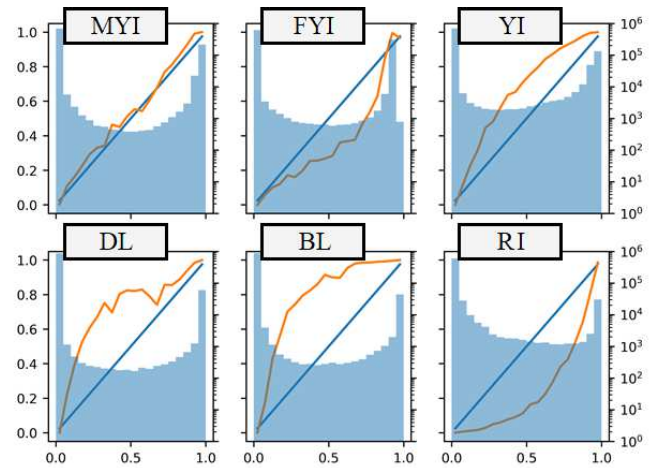

Figure 10: Plots to show the probability of being correct (y, left axis) as a function of the quoted output probability (x, in bins of 0.05) in orange vs the ideal case in blue for each of the sea ice types.

axis). These results can be used to correct the output probability at inference time to help reduce the potential biases when the results from two different images are used for the combined classification.

a) Temperature scaling: We apply a scaling in the logit space (log(p)) which optimises the Negative Log-likelihood (NLL) over the test data (see Figure 11, Figure 12, and Table II) and shows adequate performance for our preliminary tests on combined classification. However, in future work, we plan to expand the analysis and include a larger set of labelled test data.

TABLE II. TABLE OF THE TEMPERATURES PARAMETERS APPLIED AS A RESULT OF THE FIT DESCRIBED IN THE TEXT

Class	MYI	FYI	YI	DL	BL	RI
Single temp.	0.861					
Class temp.	0.843	0.819	1.174	1.181	1.017	0.274

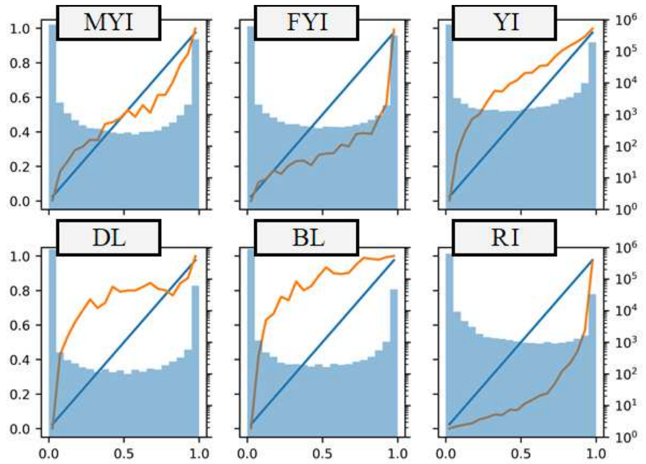

Figure 11: Plots of the calibrated probability of being correct using a single temperature scale where (y, left axis) as a function of the quoted output probability (x, in bins of 0.05) in orange vs the ideal case in blue for each of the sea ice types.

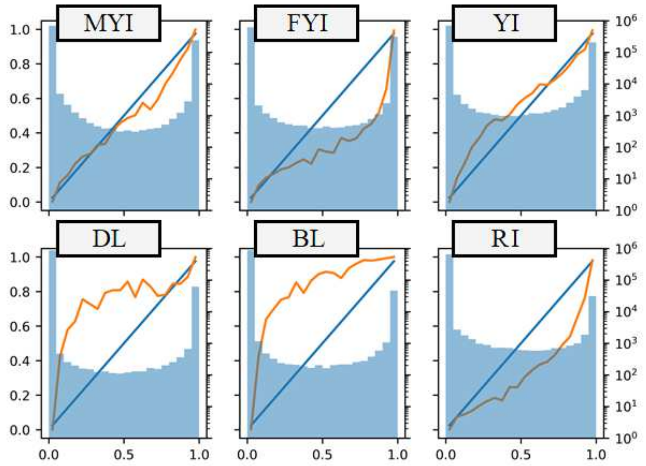

Figure 12: Plots of the calibrated probability of being correct using a separate scale for each class where (y, left axis) as a function of the quoted output probability (x, in bins of 0.05) in orange vs the ideal case in blue for each of the sea ice types.

V. CONCLUSION

In this paper, we explored the capabilities of a sea ice drift tracking algorithm for high resolution drift vector field retrieval from pairs of subsequent, co-located SAR images of the Sentinel-1 mission. Out tests deal with an image series taken between 6th and 12th December 2021 over the Arctic Ocean between Lincoln and Wandel Seas, when the ocean showed a closed cover of mainly multiyear ice.

561 drift vector fields observed manually and more than 1000 buoy validations give indications of the accuracy of sea ice drift tracking. Up to a sea ice displacement of 10 km, the one sigma error of drift estimation amounts to 132 m only. Up to 20 km of sea ice displacements, the one sigma error is 235 m. In ongoing work, we analyze accuracy of sea ice motion tracking with varying sea ice conditions i.e. in other seasons and study areas, and investigate different influencing parameters.

As an application area for sea ice drift vector fields derived from subsequent SAR acquisitions, we presented a new idea for multitemporal sea ice classification, and combine the individual classifications from our time series. We picked an example with inconsistent sea ice classification results. In most parts, doubt classified areas have been successfully corrected by our approach, even though a priori knowledge about possible class changes has not been included yet. This example showcases the strength of multitemporal sea ice classification. It provides the basis to generate sea ice classifications with increased stability and reliability, though further investigations might to be carried out in the calibration of the output of the neural network.

ACKNOWLEDGEMENT

Daten des mehrjährigen Eises vom 6.12.2021 und Meereismessungen vom 6.12.2021 bis 12.12.2021 stammen von https://www.meereisportal.de (Förderung: REKLIM-2013-04).

REFERENCES

[1] C. R. Jackson, and J. R. Apel, “Synthetic aperture radar: marine user's manual,” US Department of Commerce, National Oceanic and Atmospheric Administration, National Environmental Satellite, Data, and Information Serve, Office of Research and Applications, pp. 81-115. 2004.

[2] S. Lehner, T. Krumpen, A. Frost, R. Ressel, T. Busche, and E. Schwarz, “First Tests on Near Real Time Ice Type Classification in Antarctica,” IEEE International Geoscience and Remote Sensing Symposium (IGARSS), pp. 4876-4879, 2014.

[3] A. Frost, S. Wiehle, S. Singha, and D. Krause, „Sea Ice Motion Tracking from Near Real Time SAR Data Acquired During Antarctic Circumnavigation Expedition,” IEEE International Geoscience and Remote Sensing Symposium (IGARSS), pp. 2338-2341. 2018.

[4] A. Frost, S. Jacobsen, and S. Singha, “High resolution sea ice drift estimation using combined TerraSAR-X and RADARSAT-2 data: First tests,” IEEE International Geoscience and Remote Sensing Symposium (IGARSS), pp. 342-345. 2017.

[5] E. De Castro, C. Morandi. "Registration of translated and rotated images using finite Fourier transforms." IEEE Transactions on Pattern Analysis & Machine Intelligence 5, pp. 700-703. 1987.

[6] D. Murashkin, and A. Frost, “Arctic Sea Ice Mapping Using Sentinel-1 SAR Scenes with a Convolutional Neural Network,” IEEE International Geoscience and Remote Sensing Symposium, pp. 5660-5663. 2021.

[7] R. Scheiber, F. De Zan, P. Prats, L. S. A. Araujo, M. Künemund, and L. Marotti, „Interferometric sea ice mapping with TanDEM-X: First experiments,” Geoscience and Remote Sensing Symposium (IGARSS), IEEE International, pp. 3594-3597, 2011.

[8] J. Karvonen. Operational SAR-based sea ice drift monitoring over the Baltic Sea. In: Ocean Science 8.4: 473. 2012.

[9] T. Hollands. Motion tracking of sea ice with SAR satellite data. Diss. Universität Bremen, 2012.

[10] T. Hollands, S. Linow, and W. Dierking, “ Reliability measures for sea ice motion retrieval from synthetic aperture radar images,”. IEEE Journal of selected topics in applied earth observations and remote sensing, 8(1), 67-75. 2014.

[11] D. M. Demchev, V. V. Kharchenko, O. M. Andeeva, P. V. Korobov, and L.E. Eriksson, “Improving Sea Ice Drift Retrieval from SAR Images Using Phase-and Cross-Correlation Techniques,” IEEE Conference of Russian Young Researchers in Electrical and Electronic Engineering (ElConRus), pp. 1378-1381. 2020.

[12] R. B. Blackman, and J. W. Tukey. Particular pairs of windows. In: The measurement of power spectra, from the point of view of communications engineering. Dover, New York 1959, S. 95–101. 1959.

[13] K. G. Derpanis, “The Gaussian Pyramid”. 2005.

[14] Ye, Y.; Shokr, M.; Heygster, G. and Spreen, G. (2016), Improving multiyear ice concentration estimates with ice drift, Remote Sensing, 8(5), 397, doi:10.3390/rs8050397

[15] Ye, Y.; Heygster, G. and Shokr, M. (2016), Improving multiyear ice concentration estimates with air temperatures, IEEE Transactions on Geoscience and Remote Sensing, 54(5), 2602–2614, doi:10.1109/TGRS.2015.2503884.

[16] Nicolaus, M.; Arndt, S.; Hoppmann, M.; Krumpen, T.; Nicolaus, A.; Bartsch, A. (2017): Sea ice drift, surface temperature, and barometric pressure on sea ice from Surface Velocity Profiler measurements. Alfred Wegener Institute, Helmholtz Center for Polar and Marine Research, Bremerhaven, doi:10.1594/PANGAEA.875652.

[17] Z. Zhou, M. M. R. Siddiquee, N. Tajbakhsh, and J. Liang, “Unet++: Redesigning skip connections to exploit multiscale features in image segmentation,” IEEE transactions on medical imaging, 39(6), 1856-1867. 2019.

[18] C. Guo, G. Pleiss, Y. Sun, and K.Q. Weinberger, K., “On calibration of modern neural networks,” International conference on machine learning (pp. 1321-1330). PMLR. 2017.